Supporting Information

Giant room-temperature spin-orbit torque in a bismuthate superconductor

Anthony L. Edgeton[1], Isaac A. Harris[2], Neil G. Campbell[3], Yahong Chai[4], Marcel M. Mazur[5], Gautam Gurung[6], Xiaoxi Huang[7], Sandhya Susarla[8], Evgeny Y Tsymbal[6], Daniel C. Ralph[5,9], Tianxiang Nan[4], Mark S. Rzchowski[3], Ramamoorthy Ramesh[2,7], and Chang-Beom Eom[1*]

[1] Department of Materials Science and Engineering, University of Wisconsin-Madison, Madison, Wisconsin 53706, USA.
[2] Department of Physics, University of California, Berkely, California 94720, USA
[3] Department of Physics, University of Wisconsin-Madison, Madison, Wisconsin 53706, USA
[4] School of Integrated Circuits and Beijing National Research Center for Information Science and Technology (BNRist), Tsinghua University, Beijing 100084, China
[5] Department of Physics, Cornell University, Ithaca, NY 14853, USA
[6] Department of Physics and Astronomy & Nebraska Center for Materials and Nanoscience, University of Nebraska, Lincoln, NE 68588, USA
[7] Department of Materials Science and Engineering, University of California, Berkely, California 94720, USA
[8]School for Engineering of Matter, Transport, and Energy, Arizona State University, Arizona 85281, USA
[9]Kavli Institute at Cornell for Nanoscale Science, Ithaca, NY 14853, USA

*Corresponding author: eom@engr.wisc.edu

Note 1. Structural characterization.

Note 2. Magnetic characterization.

Note 3. Theory calculations

Note 4. ST-FMR analysis

Note 5. Non-linear Hall analysis

Note 6. Thermoelectric effects in BPBO/Pt(Co) devices

Note 7. Self-torque in Pt(Co) control samples

Note 8. Field dependence of switching in BPBO/Pt(Co) devices

Note 9. Shunting factor in BPBO/Pt(Co)

Note 10. Comparison of spin source materials

Note 1. Structural characterization.

Fig. S1a-c show XRD for LSMO (35 nm)/BPBO (65 nm) bilayers on (001) STO grown *in-situ* by pulsed laser deposition. For convenience each complex perovskite structure is treated as pseudocubic. Rocking curves of (002) peak for both BPBO (Fig. S1a) and LSMO (Fig. S1b) show good crystallinity with FWHM of 0.02°. From symmetric θ-2θ scans of the (002) peaks for BPBO, STO, and LSMO in Fig. S1c we estimate the out-of-plane lattice parameters, c, of BPBO and LSMO to be 4.27Å and 3.86Å. Keisig fringes indicate smooth surfaces. The lattice parameter of BPBO is similar to theoretical bulk values and optimized thin films confirming the high quality, fully relaxed state. The smaller out-of-plane lattice parameter of LSMO

compared to bulk is due to the tensile strain of LSMO on STO. Further structural characterization is done using STEM. Fig. S1d shows an image with zone axis aligned to the BPBO film while Fig. S1e is aligned to both LSMO and STO. The 2mRad difference in alignment could be due to sample bending or tilting of the BPBO epitaxial relationship. Although the mismatch between BPBO and LSMO is large, the interface appears well ordered with crystallinity of both the relaxed BPBO and LSMO are maintained approaching the interface.

XRD for BPBO/(Pt/Co) is shown in Fig. S2. BPBO (20nm) is grown by 90° off-axis magnetron sputtering. Pt/Co is grown *ex-situ* by DC magnetron sputtering in multilayers. Rocking curve in the inset of Fig. 2Sa matches BPBO grown by PLD with FWHM of 0.02°. Out-of-plane θ-2θ scan shown in Fig. S2a gives lattice parameter c of 4.27Å and shows no change with addition of Pt(Co) multilayers. X-ray reflectivity (XRR) is shown in Fig. S2b. Two distinct periodicities indicate an abrupt interface between the 20nm BPBO (short periodicity) and 6.2 nm Pt(Co) layer (long periodicity). The inset of Fig. S2b shows atomic force microscopy image of the surface of a BPBO sample indicating a smooth surface with RMS roughness ~4Å.

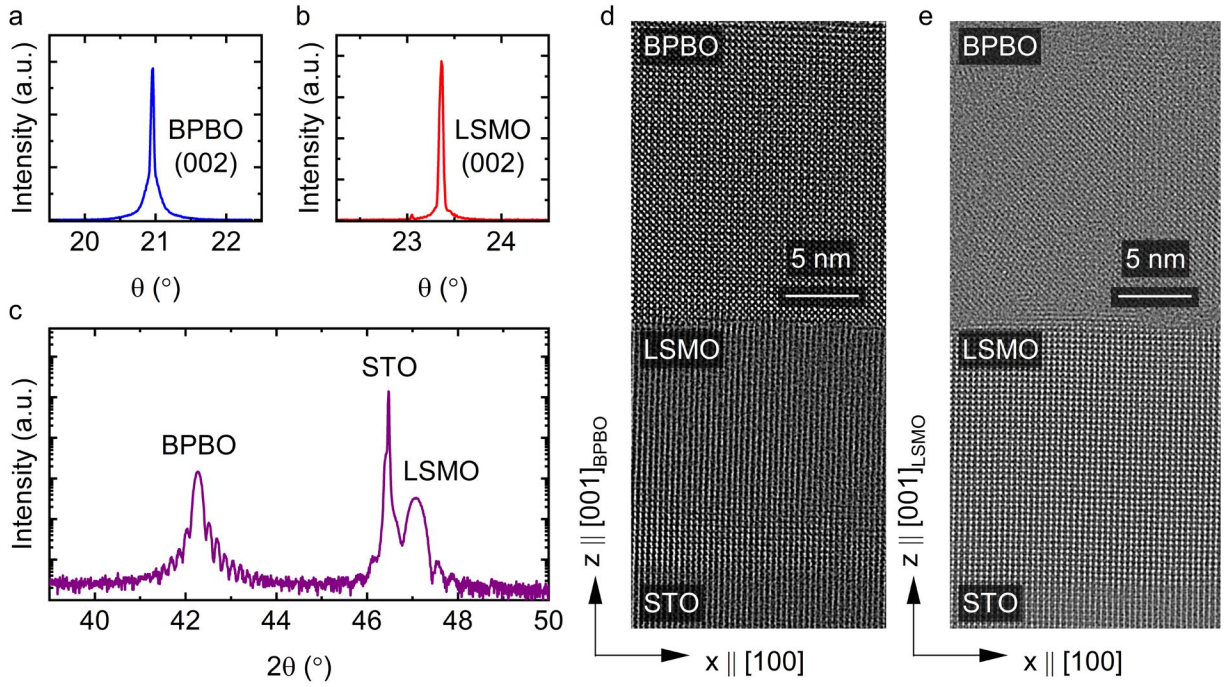

Figure S1 | Structural characterization of LSMO/BPBO bilayers deposited on (001) STO. a, X-ray diffraction rocking curve of (002) BPBO peak. **b,** Rocking curve of (002) LSMO peak. **c,** Symmetric θ-2θ scan around labeled (002) peaks of BPBO, STO, and LSMO. **d,** Scanning transmission electron microscope image of BPBO/LSMO on (001) STO aligned to BPBO **e,** Image aligned to LSMO. Rotation is 2mRad about the x-axis.

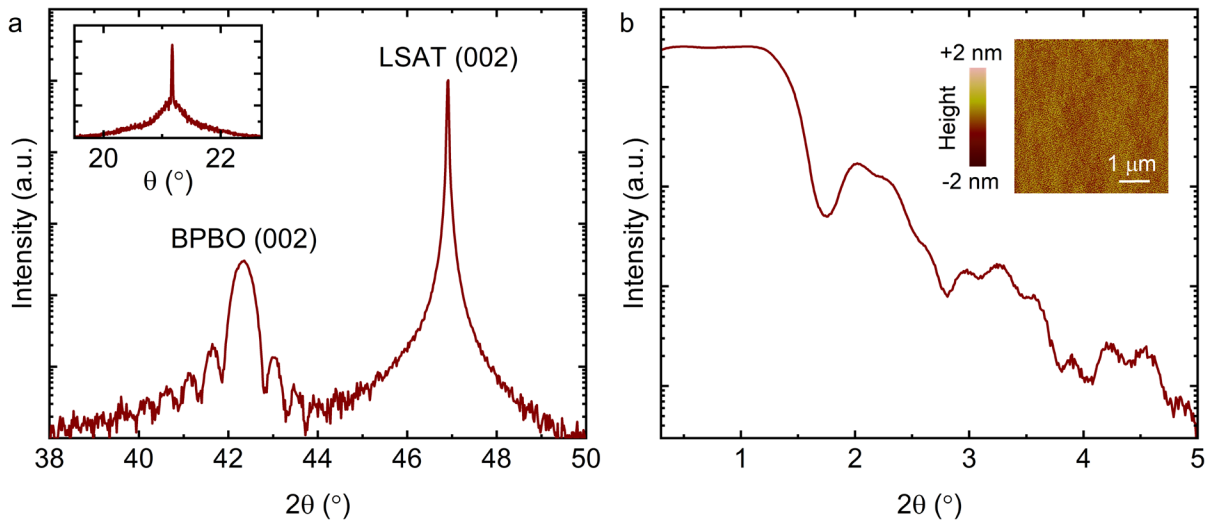

Figure S2 | Structural and surface characterization of BPBO/Pt(Co) deposited on (001) LSAT. a, X-ray diffraction symmetric θ-2θ scan around labeled (002) peaks of BPBO, and LSAT. Inset shows a rocking curve of (002) BPBO peak. **b,** X-ray reflectivity of BPBO (20 nm)/Pt(Co) (6.2 nm). Inset shows atomic force microscopy image of BPBO surface.

Note 2. Magnetic characterization.

In-plane and out-of-plane magnetic hysteresis loops shown in Fig. S3 were carried out in a Quantum Design MPMS 3 for both BPBO/LSMO bilayers and BPBO/Pt(Co) samples. In-plane magnetic fields are applied along the [100] crystallographic direction of the substrates. LSMO exhibits an in-plane magnetic hard axis. The in-plane saturation magnetization is about 400 emu/cm^3. The Pt(Co) magnetization shows an out-of-plane magnetic hard axis. The out-of-plane saturation magnetization is 400 emu/cm^3. The anisotropy field is estimated as 280mT.

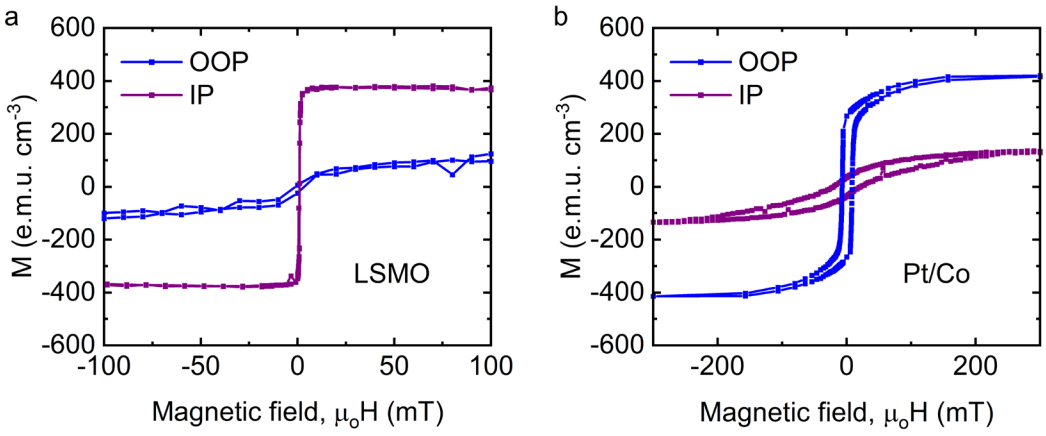

Figure S3 | Magnetic characterization. a, Superconducting quantum interference device measurements of magnetic hysteresis loops for both in-plane and out-of-plane field directions at 300K for LSMO/BPBO and **b,** BPBO/Pt(Co)

Note 3. Theory calculations

First-principles density functional theory calculations with fully relativistic ultrasoft pseudopotentials[1] were performed with Quantum ESPRESSO[2]. The exchange and correlation effects were treated within the generalized gradient approximation (GGA)[3]. The plane-wave cut-off energy of 52 Ry and a $16 \times 16 \times 16$ k-point mesh in the irreducible Brillouin zone were used in the calculations. The lattice parameter obtained by fitting Murnaghan equation of state is $a = 4.36$ Å [4]. Spin-orbit coupling was included in all electronic structure calculations until mentioned otherwise.

Tight-binding Hamiltonians are constructed using PAOFLOW[5] code based on the projection of the pseudo-atomic orbitals (PAO)[6,7] from the non-self-consistent calculations with a $16 \times 16 \times 16$ *k*-point mesh. The spin Hall conductivities were calculated using the tight-binding Hamiltonians with a $48 \times 48 \times 48$ *k*-point mesh by the adaptive broadening method to get the converged values. The spin Hall conductivity is given by

$$\sigma_{ij}^{k} = \frac{e^2}{\hbar} \int \frac{d^3\vec{k}}{(2\pi)^3} \sum_{n} f_{n\vec{k}} \Omega_{n,ij}^{k}(\vec{k}),$$

$$\Omega_{n,ij}^{k}(\vec{k}) = -2Im \sum_{n \neq n'} \frac{\langle n\vec{k}|J_i^k|n'\vec{k}\rangle\langle n'\vec{k}|v_j|n\vec{k}\rangle}{\left(E_{n\vec{k}} - E_{n'\vec{k}}\right)^2},$$

where $f_{n\vec{k}}$ is the Fermi-Dirac distribution for the *n*th band, $J_i^k = \frac{1}{2}\{v_i, s_k\}$ is the spin current operator with spin operator s_k, $v_j = \frac{1}{\hbar}\frac{\partial H}{\partial k_j}$ is the velocity operator, and $i, j, k = x, y, z$. $\Omega_{n,ij}^{k}(\vec{k})$ is referred to as the spin Berry curvature in analogy to the ordinary Berry curvature.

We first consider the cubic structure for $BaPbO_3$ with lattice constant 4.36 Å. Fig. S4 shows the orbital-projected band structure for all the elements. The oxygen p orbital has the largest contribution to the bands around the Fermi level. By symmetry, only conventional spin Hall conductivity (SHC) components (σ_{xy}^{z}) are finite in the cubic $BaPbO_3$. The calculated value is $\sigma_{xy}^{z} = 25\ \frac{\hbar}{e}\ (\Omega cm)^{-1}$ at the Fermi energy. Fig. S5 shows the variation of the SHC near the Fermi level. The wide band above the Fermi level leads to slowly varying SHC. The major contribution at the Fermi energy comes from the *R* point as seen from the distribution of the spin Berry curvature Ω_{xy}^{z} in the [110] plane of the Brillouin zone (Fig. S6). This is due to the small splitting of the bands near the *R* point driven by spin-orbit coupling. Taking into account effects of possible octahedral rotations in the $BaPbO_3$ does not change the SHC significantly compared to the cubic phase. Finally, using the virtual crystal approximation for the substitutional doping of Pb by Bi, we find the variation of the SHC with respect to the energy level remains similar and the addition of Bi simply raises the Fermi energy. The calculated value is $\sigma_{xy}^{z} = 17\ \frac{\hbar}{e}\ (\Omega cm)^{-1}$ at the Fermi energy for $BaPb_{0.75}Bi_{0.25}O_3$.

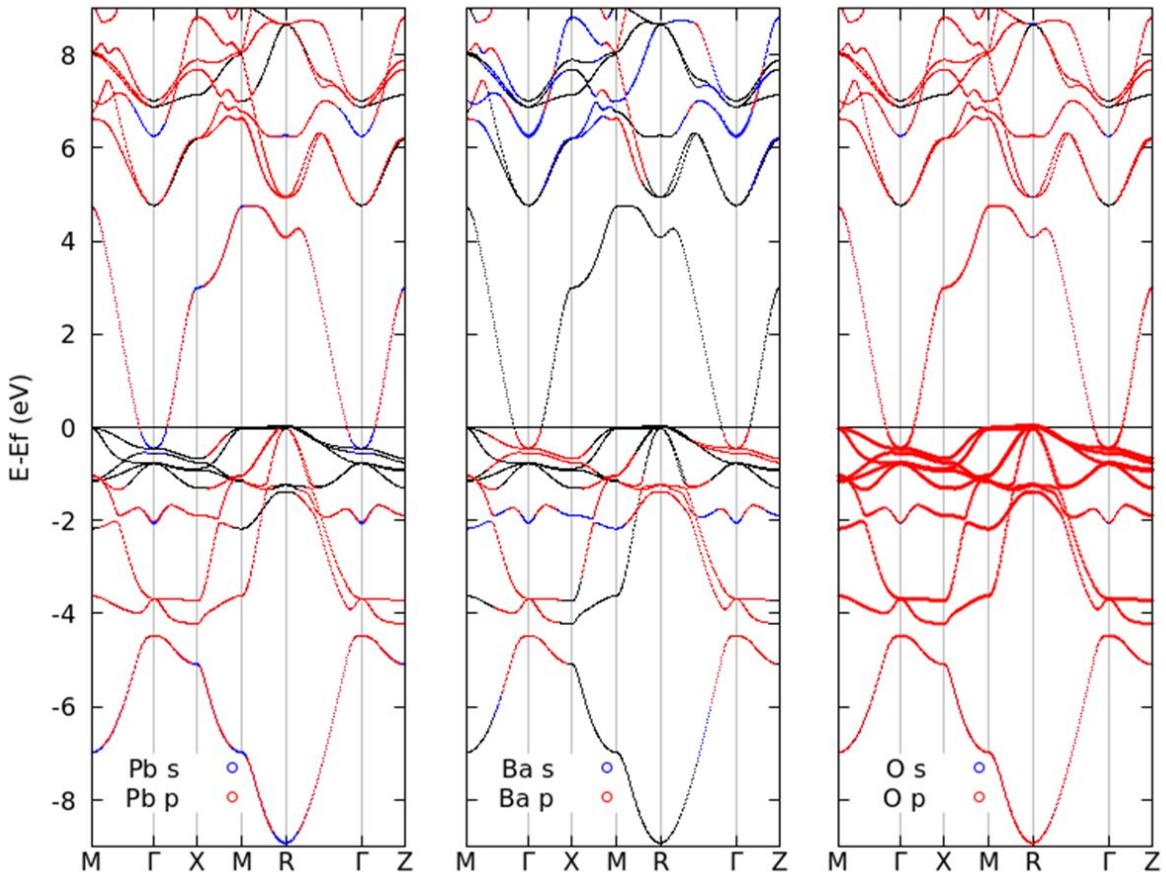

Figure S4 | Orbital projected band structure of the cubic $BaPbO_3$ for Ba, Pb and O.

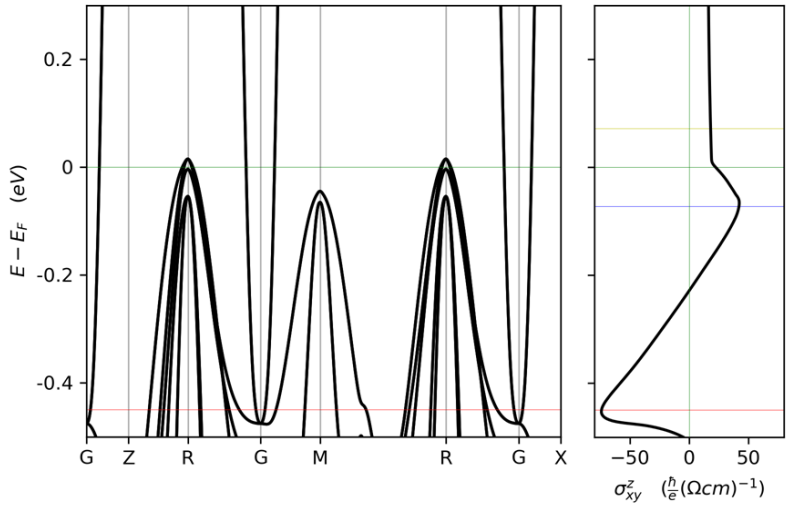

Figure S5 | Variation of spin Hall conductivity σ_{xy}^z around the Fermi energy (indicated by the green line).

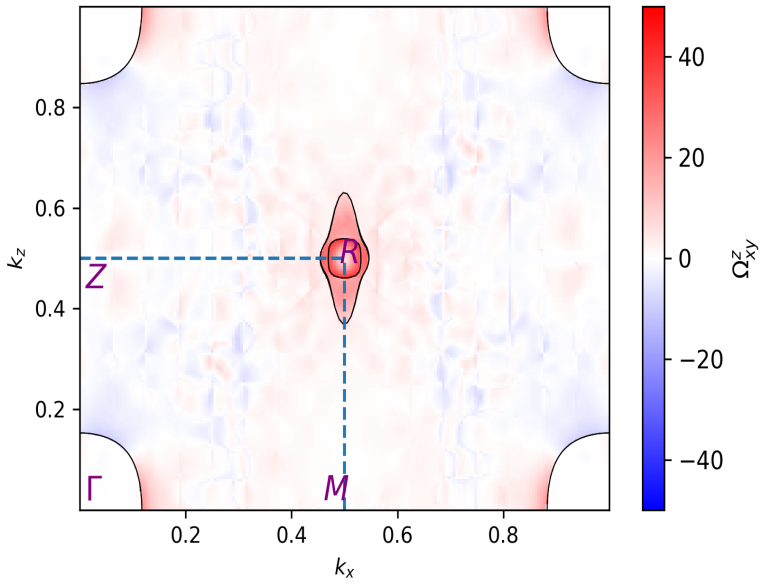

Figure S6 | Variation of spin Berry curvature at the Fermi energy in the [110] plane of the Brillouin zone.

Note 4. ST-FMR analysis

It is well known that many artifacts can contribute to the symmetric signal in traditional, longitudinal ST-FMR such as spin pumping (SP) and the inverse spin Hall effect (ISHE), the anomalous Nernst effect (ANE), and the spin Seebeck effect (SSE). We use transverse Hall measurements as presented by Karimeddiny et al[8] to calculate the effects of these artifacts on our longitudinal ST-FMR signal. The applied radio-frequency current $I_{\mathrm{rf}}e^{-i\omega t}$ excites the unit magnetization $\hat{m}$ of the BPBO into precession governed by the LLGS equation, shown below

$$\dot{\hat{m}} = \gamma\hat{m} \times \frac{dF}{d\hat{m}} + \alpha\hat{m} \times \dot{\hat{m}} + \vec{\tau}_{\mathrm{FL}} + \vec{\tau}_{\mathrm{DL}} + \vec{\tau}_{\mathrm{Oe}}$$

Where γ and F are the gyromagnetic ratio and free energy which govern precession about the external field B, α is the Gilbert damping, and $\vec{\tau}_{\mathrm{FL,DL,Oe}}$ are the field-like, damping-like, and Oersted torques driving $\hat{m}$ into precession. The resonant field which maximizes deflection of the magnetization is the field B_0 which solves the Kittel equation $\omega = \gamma\sqrt{B(B+\mu_0 M_{\mathrm{eff}})}$ where $\mu_0 M_{\mathrm{eff}} = \mu_0 M_{\mathrm{s}} - 2K_{\perp}/M_{\mathrm{s}}$ where μ_0 is the permeability of free space, M_{s} is the saturation magnetization, and $K_{\perp}$ is the anisotropy term which keeps the magnetization in-plane. In practice, M_{eff} is extracted by plotting the observed B_0 against the applied frequency ω as in Fig. S4b. Solving for the magnetization near the resonant field B_0 in the reference frame where the y-axis is parallel to the external field and the z-axis is normal to the sample surface, we can find the components of the precessing magnetization

$$m_x(t) = m_x e^{-i\omega t} \text{ with } m_x = \frac{-\omega_2\tau_z + i\omega\tau_x}{-(B-B_0)\gamma\omega^+ + i\omega\alpha\omega^+}$$

$$m_z(t) = m_z e^{-i\omega t} \text{ with } m_z = \frac{\omega_1\tau_x + i\omega\tau_z}{-(B-B_0)\gamma\omega^+ + i\omega\alpha\omega^+}$$

Where $\omega_2 = \gamma B + \mu_0 M_{\text{eff}}$, $\omega_1 = \gamma B$, $\omega^+ = \omega_1 + \omega_2$, $\tau_x = (\vec{\tau}_{\text{FL}} + \vec{\tau}_{\text{DL}} + \vec{\tau}_{\text{Oe}}) \cdot \hat{x} = -\tau_{\text{DL}}^0 \cos\phi$, and similarly, $\tau_z = (\tau_{\text{Oe}}^0 - \tau_{\text{FL}}^0)\cos\phi$, and ϕ is the angle between the external magnetic field and the direction of current flow. The torques from the Oersted field and the spin-polarized current are opposite in sign assuming a positive SOT efficiency due to the growth order: LSMO is underneath the BPBO. The torques can be written in terms of the charge current density J_e in the BPBO and spin-torque efficiencies ξ_{FL}, and $\xi_{\text{DL}} = \theta_{\text{SOT}}$:

$$\tau_{\text{DL}}^0 = \xi_{\text{DL}} \frac{\mu_B J_e}{e M_s t_{\text{FM}}},\ \tau_{\text{FL}}^0 = \xi_{\text{FL}} \frac{\mu_B J_e}{e M_s t_{\text{FM}}},\ \text{and}\ \tau_{\text{Oe}}^0 = \frac{\mu_0 \gamma J_e t_{\text{NM}}}{2}$$

Where μ_B is the Bohr magneton, e is the elementary charge, and t_{FM} and t_{SOC} are the thicknesses of the ferromagnetic LSMO layer and non-magnetic BPBO layer respectively. The precessing magnetization and the anisotropic and spin Hall magnetoresistance effects (MR), anomalous hall effect (AHE), and planar hall effect (PHE), combined with the alternating current, give us the following mixing voltages V_{XX}^{mix} and V_{XY}^{mix} which are measured from the bias tee and the hall contact pads respectively.

$$V_{XX}^{\text{mix}} = -R_{\text{MR}} \sin(2\phi)\, I_{\text{rf}} \frac{1}{2} \text{Re}[m_x]$$

$$V_{XY}^{\text{mix}} = R_{\text{PHE}} \cos(2\phi)\, I_{\text{rf}} \frac{1}{2} \text{Re}[m_x] - R_{\text{AHE}} I_{\text{rf}} \frac{1}{2} \text{Re}[m_z]$$

Where $R_{\text{MR}} = R_{\text{AMR}} + R_{\text{SMR}}$, R_{PHE}, and R_{AHE} are the coefficients for anisotropic and spin Hall magnetoresistances, planar Hall effect, and anomalous Hall effect respectively. The real parts of the magnetization components contain the symmetric and antisymmetric Lorentzian shapes around the resonant field B_0:

$$\text{Re}[m_x] = \frac{\cos\phi}{\omega^+ \alpha}\left[\tau_{\text{DL}}^0 S(B) + \left(\tau_{\text{FL}}^0 - \tau_{\text{Oe}}^0\right)\frac{\omega_2}{\omega} A(B)\right]$$

$$\text{Re}[m_z] = \frac{\cos\phi}{\omega^+ \alpha}\left[\tau_{\text{DL}}^0 \frac{\omega_1}{\omega} A(B) - \left(\tau_{\text{FL}}^0 - \tau_{\text{Oe}}^0\right) S(B)\right]$$

Where $S(B) = \Delta^2/((B - B_0)^2 + \Delta^2)$, $A(B) = (B - B_0)\Delta/((B - B_0)^2 + \Delta^2)$, and $\Delta = \alpha\omega/\gamma$. The linearity of $\Delta(\omega)$ can be seen in Fig. S4c. If we incorporate the effects of artifacts, we find that the effects of spin pumping and any thermal gradient will be proportional to the amplitude of the precession of the magnetization[8], and near the resonant field will take the form $\vec{E}_{\text{art}} = E_{\text{art}}^0 S(B) \cos^2\phi\, \hat{x}$. Through geometrical considerations of SP and ISHE, SSE and ISHE, and NE, it can be shown that the longitudinal voltages add the following terms to the longitudinal and transverse mixing voltages:

$$V_{XX}^{\text{mix/art}} = V_{XX}^{\text{mix}} + \sin(2\phi) cos\phi\, S(B)\, E_{\text{art}}^0 \frac{L}{2}$$

$$V_{XY}^{\text{mix/art}} = V_{XY}^{\text{mix}} + (\cos(2\phi) cos\phi + cos\phi) S(B)\, E_{\text{art}}^0 \frac{W}{2}$$

Where L and W are the length and width of the sample bar in the ST-FMR device. By separating the symmetric and antisymmetric Lorentzian fits at different field angles, we arrive at the following dependence on ϕ of the longitudinal symmetric and antisymmetric fit amplitudes from $V_{XX}^{\text{mix/art}} = V_S^{XX} + V_A^{XX}$ as well as the transverse symmetric and antisymmetric fit amplitudes from $V_{XY}^{\text{mix/art}} = V_S^{XY} + V_A^{XY}$:

$$V_S^{XX}(\phi) = S_{XX}^{\text{MR/art}} \sin(2\phi)\cos\phi, \quad V_A^{XX}(\phi) = A_{XX}^{\text{MR}} \sin(2\phi)\cos\phi$$

$$V_S^{XY}(\phi) = S_{XY}^{\mathrm{PHE/art}} \cos 2\phi \cos\phi + S_{XY}^{\mathrm{AHE/art}} \cos\phi$$

$$V_A^{XY}(\phi) = A_{XY}^{PHE} \cos 2\phi \cos\phi + A_{XY}^{AHE} \cos\phi$$

$V_{XX}^{\mathrm{mix/art}}$ and $V_{XY}^{\mathrm{mix/art}}$ traces from longitudinal and transverse ST-FMR experiments, such as those shown in Fig. S7, allow us to measure the 6 amplitudes above. These can depend on MR, PHE, AHE, and the artifact field. We can then write the dimensionless ratio $\eta = (\tau_{\mathrm{DL}}^0/(\tau_{\mathrm{FL}}^0 - \tau_{\mathrm{Oe}}^0))\sqrt{\omega_1/\omega_2}$ three different ways:

$$\eta = \frac{S_{XX}^{\mathrm{MR,art}} - E_{\mathrm{art}\frac{L}{2}}^0}{A_{XX}^{MR}} = \frac{S_{XY}^{\mathrm{PHE,art}} - E_{\mathrm{art}\frac{W}{2}}^0}{A_{XY}^{\mathrm{PHE}}} = \frac{A_{XY}^{\mathrm{AHE}}}{S_{XY}^{\mathrm{AHE,art}} - E_{\mathrm{art}\frac{W}{2}}^0}$$

Using the above equations, η can be used to calculate the SOT efficiency

$$\theta_{\mathrm{SOT}} = \eta\left(\xi_{\mathrm{FL}} - \frac{eM_s\mu_0\gamma t_{\mathrm{FM}} t_{\mathrm{NM}}}{2\mu_B}\right)\sqrt{1 + \frac{\mu_0 M_{\mathrm{eff}}}{B_0}}$$

The redundancy in these equations allows us to calculate the longitudinal artifact voltage in our samples $E_{\mathrm{art}\frac{L}{2}}^0$, and we find $E_{\mathrm{art}\frac{L}{2}}^0 \approx 0.3\,\mu\mathrm{V}$, whereas we find $S_{XX}^{\mathrm{MR,art}} \approx 6\,\mu\mathrm{V}$. Therefore, when calculating the magnitude of the SOT efficiency in longitudinal ST-FMR, we can use $\eta = S_{XX}^{\mathrm{MR,art}}/A_{XX}^{MR}$ and know that the systematic uncertainty from artifacts is only 5%. Furthermore, by measuring η over a range of t_{FM}, we can calculate ξ_{FL} and find $\xi_{\mathrm{FL}} \approx 0.06 \pm 0.04$ in Fig. S8, leading us to conclude that the field-like torques generated by the spin-current are small in comparison to the damping-like torques, which we find to be $\theta_{\mathrm{SOT}} \approx 1.7 \pm 0.3$.

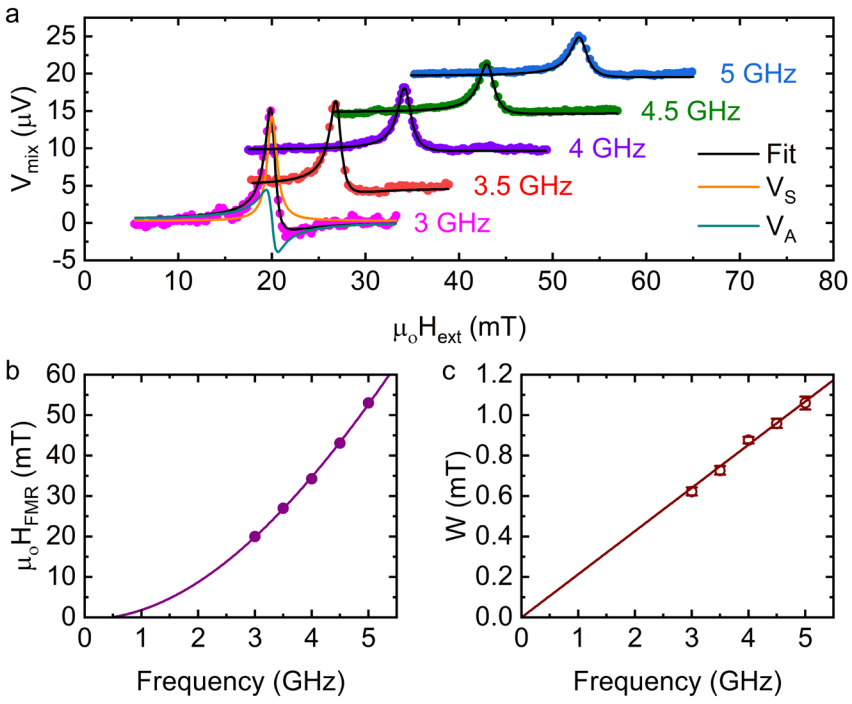

Figure S7 | ST-FMR a, Resonance spectrum with varying frequency each fit with symmetric (V_S) and antisymmetric (V_A) Lorentzian functions. **b,** Resonance magnetic field, H_{FMR}, shift

dependence on frequency fit to Kittel formula giving $M_{eff} = 390\,kA/m$. **c,** Frequency dependence of linewidth broadening, W, with a linear fit to extract Gilbert damping parameter $\alpha = 0.008$.

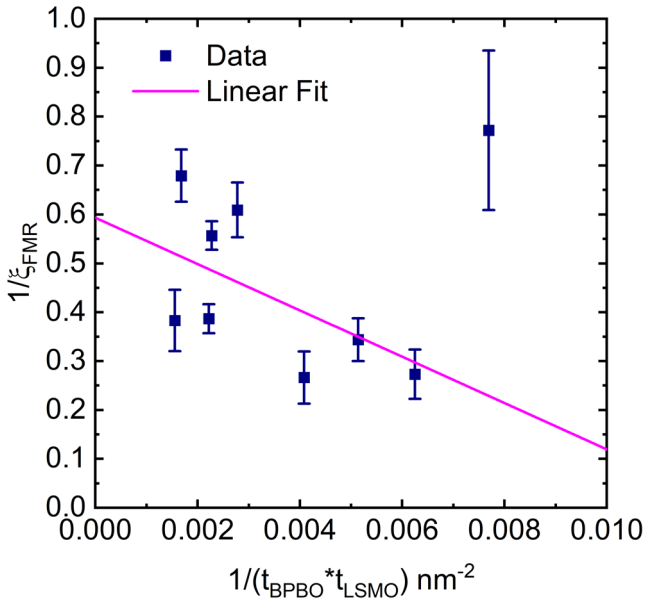

Figure S8 | ST-FMR with varying thickness. Thickness dependence of SOT efficiency calculated using lineshape analysis. Data is linearly fit and damping-like torque is calculated from the intercept while the field-like torque is calculated from the slope.

Note 5. Non-linear Hall analysis

Our DC measurement technique for out-of-plane magnetized devices (Pt(Co) multilayers) was based on the non-linear Hall I-V characteristic of the multilayer system. To quantify the spin torque, we measured the quadratic component of the Hall voltage with respect to current caused by the current-induced change in Hall resistance due to manipulation of the Co magnetic moment direction.

Specifically, spin torque of BPBO/Pt(Co) was determined via Hall measurements carried out on 100μm long and 10μm wide Hall bars in a Quantum Design PPMS. Devices were patterned along both the [100] and [010] crystallographic directions. Current up to I_{max} = 9 mA was sourced by linked Keithley 6221 and 2182a devices which provided linearly-spaced current sweeps from - I_{max} to I_{max} to - I_{max}, with voltage read at each step. Such measurements were performed at fixed in-plane magnetic fields aligned parallel to the current direction.

Measuring the sample with the same magnetic state for both polarities is of utmost importance. To ensure this as best we could, measurements were performed after the sample had been rotated from an out-of-plane magnetic field to in-plane in a constant-magnitude field. Then the magnetic field was set to a magnitude of 2 T before commencing measurements of either polarity and measurements were taken with decreasing field magnitude. This was especially important for the second polarity measured, as spin-torque measurements near $|H_{ext}| = H_k$ can cause significant domain formation.

To extract the quadratic signal, we combined IV sweeps at positive and negative polarities. In theory, this isolates the quadratic component by removing the linear component. However, there were other higher-

order contributions as well. To extract only the quadratic component, the data were fit to a 5th order polynomial, and only the quadratic coefficient was taken. Breaking down the IV curve, we have

$$V_H = IR_H = IR_{AHE}\left(M_z^{avg} + \delta M_z I\right) = IR_{AHE}M_z^{avg} + I^2 R_{AHE}\delta M_z$$

where V_H is the voltage measured, R_{AHE} is the constant of proportionality between the out-of-plane magnetization and the Hall resistance, and δM_z is the constant of proportionality between the current and the change in out-of-plane magnetization. In this case $C \propto R_{AHE}\,\delta M_z$, where δM_z is more commonly referred to as b_{st}, or the effective spin-orbit field value.

The spin-torque values were computed from the field dependence of the quadratic component from field values below 1.5 T, but still in the high-field limit, according to

$$C = -\frac{1}{2}\frac{R_{AHE}\delta M_z}{\mu_0(|H_x| - H_k)}$$

where C is the quadratic contribution to the I-V curve, and $|H_x|$ is the magnitude of the in-plane field. To extract δM_z from C, we measure the anomalous Hall effect resistance with a strictly out-of-plane magnetic field.

Note 6. Thermoelectric effects in BPBO/Pt(Co) devices

Thermoelectric effects such as the anomalous Nernst-Ettingshausen effect (ANE) and spin Seebeck effect (SSE) also contribute to the non-linear Hall behavior. Fabrication defects, especially near corners of the device, produce current generated in-plane thermal gradients of the form ∇T_x. The ANE in Pt(Co) generates a non-linear Hall contribution, C_{Thermo}, which is dependent on the out-of-plane magnetic moment, mimicking the in-plane field dependence of the AHE. When magnetization is fully out-of-plane, C_{Thermo} is maximized and there no SOT contributions. Fig. S9a shows the quadratic non-linear Hall behavior while applying a fully saturating out-of-plane magnetic field, $\mu_0 H_z$, which gives the C_{Thermo} contribution. The proportional in-plane C_{Thermo} dependence is plotted in Fig. S9b and its impact on the measurement is shown in Fig. S9c.

Additionally, due to the difference in thermal conductivity of BPBO and air, out-of-plane thermal gradients arise of the form ∇T_z. This gives rise to the SSE which generates an out-of-plane spin current, j_s, and in conjunction with the inverse spin Hall effect in Pt or BPBO produces a transverse voltage proportional to I^2. ANE and SSE due to ∇T_z depend on magnetization direction and saturate with a fully in-plane magnetic moment. Because the SOT signal is suppressed at higher in-plane magnetic field, a constant offset is attributed to purely ANE and SSE effects. After subtracting ∇T_x contributions in Fig. S9c the data is linearized and plotted in Fig. S9d. The extrapolated intercept representing an infinite in-plane field is due to thermoelectric effects. The estimated in-plane field dependence is plotted in Fig. S9e producing a constant offset for high-field measurements. After subtracting all thermoelectric contributions due to ∇T_x and ∇T_z the final corrected data set is fit using Equation 3 in the main text and plotted with the raw measured data in Fig. S9f.

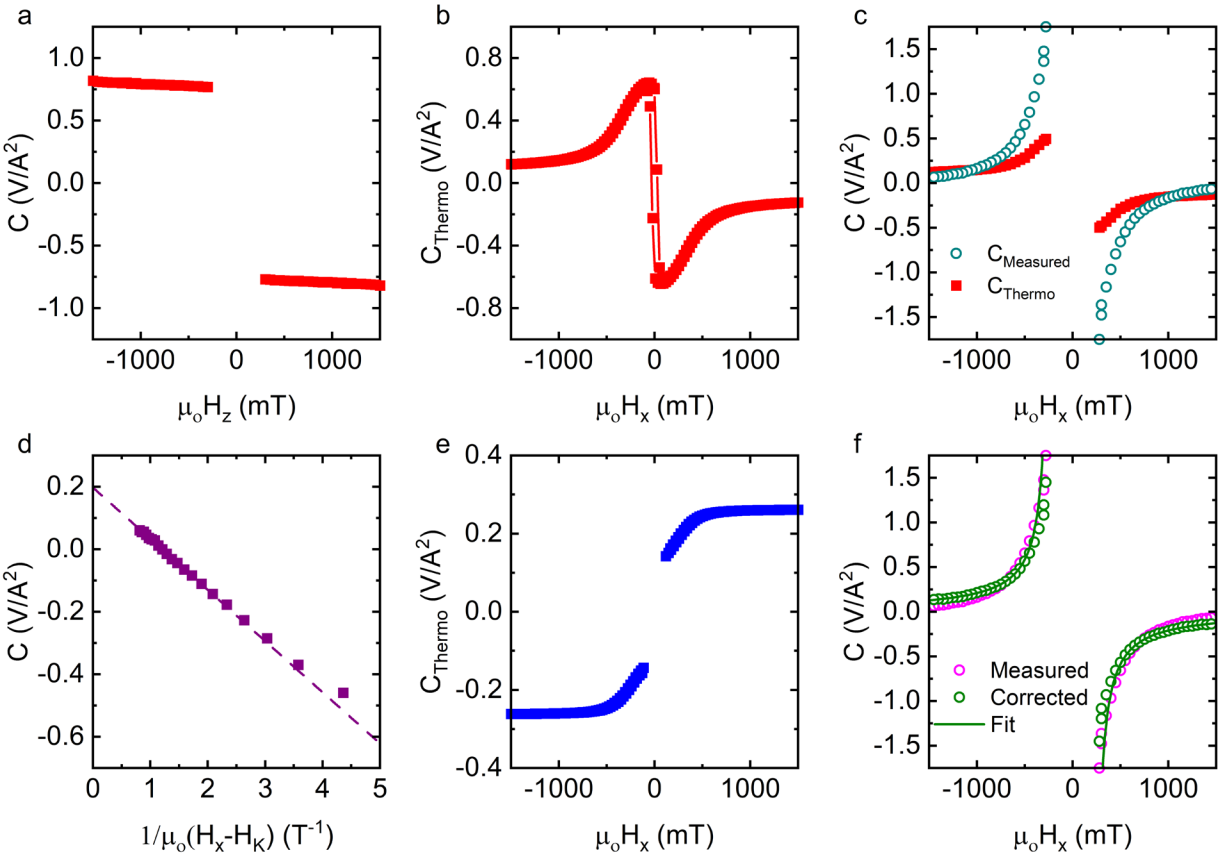

Figure S9 | Estimation of thermoelectric effects in non-linear Hall measurements of BPBO/Pt(Co). a, Out-of-plane field dependence of quadratic I-V coefficient. **b,** Estimated dependence of thermoelectric contributions from (a) as a function of in-plane field. **c,** Comparison of the measured quadratic V_{even} coefficient to the estimated thermoelectric contribution. **d,** Linearized quadratic I-V signal after subtracting (b) as a function of $1/(\mu H_x - \mu H_K)$ **e,** Estimated thermoelectric contributions from the intercept of (d) plotted as a function of applied in-plane field. **f,** Final corrected quadratic I-V signal fit to extract SOT contribution after subtracting thermoelectric effects estimated in (b) and (e) compared to the raw measured signal.

Note 7. Self-torque in Pt(Co) control samples

To test the possibility of self-torque generated in the Pt(Co) layer we fabricated a $[Pt(0.92nm)/Co(0.4nm)]_4Pt(0.92nm)$ control sample on (001) LSAT. Identical experiments as in Supplemental Note 6 were performed to remove thermoelectric contributions. The Hall resistance measured as a function of out-of-plane and in-plane magnetic field is shown in the top of Fig. S10a. The sample has an out-of-plane magnetic easy axis with a slightly larger anisotropy field than samples with BPBO. The measured in-plane field dependence, $\mu_0 H_x$, of the quadratic non-linear Hall behavior is plotted in the bottom of Fig. S10a. The ∇T_x and ∇T_z contributions are extracted in Fig. S10b and S10d respectively. A large contribution in the measured non-linear Hall comes from the ANE induced from ∇T_x as shown in Fig. S10c. The corrected data set is fit and compared to the corrected data set for a sample with BPBO in Fig. S10e. The extracted damping-like effective field from Pt(Co) is found to be 0.8 Oe/mA and is subtracted from BPBO results in the main text considering current flowing through the Pt(Co) layer.

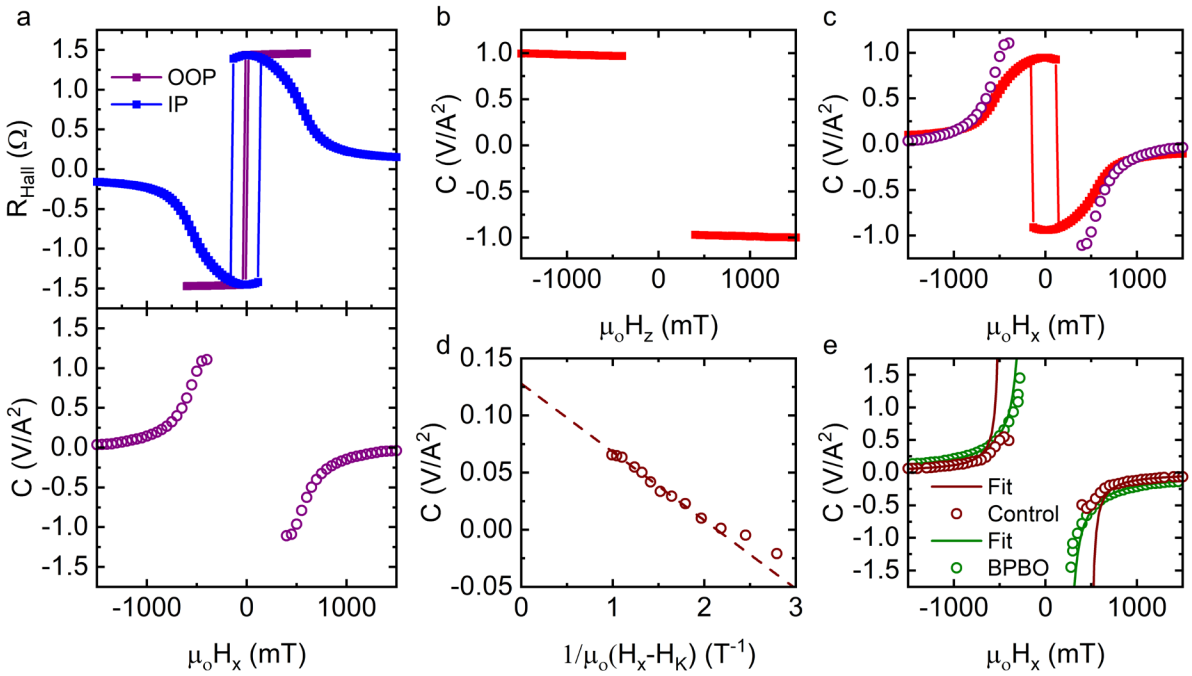

Figure S10 | Estimation of self-torque in Pt(Co) control sample deposited on (001) LSAT. **a,** Top panel shows the Hall resistance measured as a function out-of-plane and in-plane magnetic field. Bottom panel is the raw measured signal of quadratic I-V coefficient. **b,** Out-of-plane field dependence of quadratic I-V coefficient. **c,** Comparison of estimated thermoelectric contributions extracted in (b) and raw measured data in (a). **d,** Linearized data after subtracting thermoelectric effects in (c). **e,** Comparison of control sample signal to BPBO/Pt(Co) sample each free from thermoelectric contributions.

Note 8. Field dependence of switching in BPBO/Pt(Co) devices

Purely in-plane conventional SOT switching requires an additional in-plane field H_x applied parallel to the current direction to break symmetry. To determine the in-plane field dependence of deterministic switching in BPBO/Pt(Co) devices we perform full switching hysteresis loops while supplying varying H_x. The results in Fig. S11 show deterministic switching for finite H_x but not for zero field. Finite H_x cants the out-of-plane magnetic moment which in response to the current-driven in-plane torque dictates the preferred final magnetic state depending on the current direction. This causes a chirality reversal of the switching hysteresis loops observed when the sign of H_x is reversed. The change in Hall resistance is maximized and achieves nearly saturated magnetization compared to AHE measurements at ±10mT. The switching hysteresis loop shrinks at higher applied fields indicating the formation of a multidomain state.

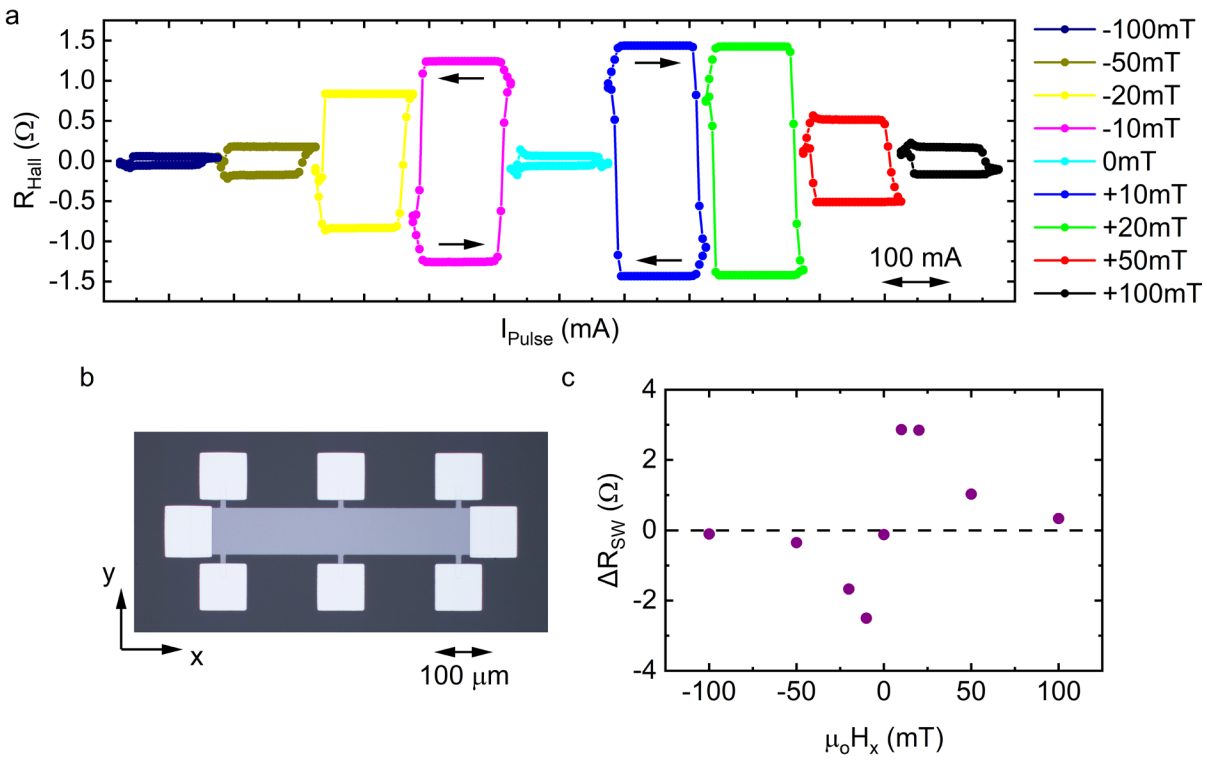

Figure S11 | Field dependence of deterministic switching in BPBO/Pt(Co). a, Current induced SOT switching at various in-plane field H_x parallel to the pulsed current direction. **b,** Micrograph of patterned device used for device switching measurements. **c,** Change in Hall resistance for each magnetic polarization direction induced by SOT switching at various in-plane fields. Change in sign represents the chirality reversal expected for SOT switching.

Note 9. Shunting factor in BPBO/Pt(Co)

The SOT efficiency in BPBO/Pt(Co) and switching current density are calculated considering current flowing only in BPBO. The sheet resistance of 20nm BPBO is shown in Fig. S12a along with the sheet resistance of the BPBO/Pt(Co) device. Using a parallel resistor model, the shunting factor, $s = t_{FM}\rho_{BPBO}/d_{BPBO}\rho_{FM}$, and its temperature dependence are calculated in Fig. S12b. The estimated amount of current in BPBO with resistivity, $\rho = 1110\ \mu\Omega cm$, is 14.8% at 300K.

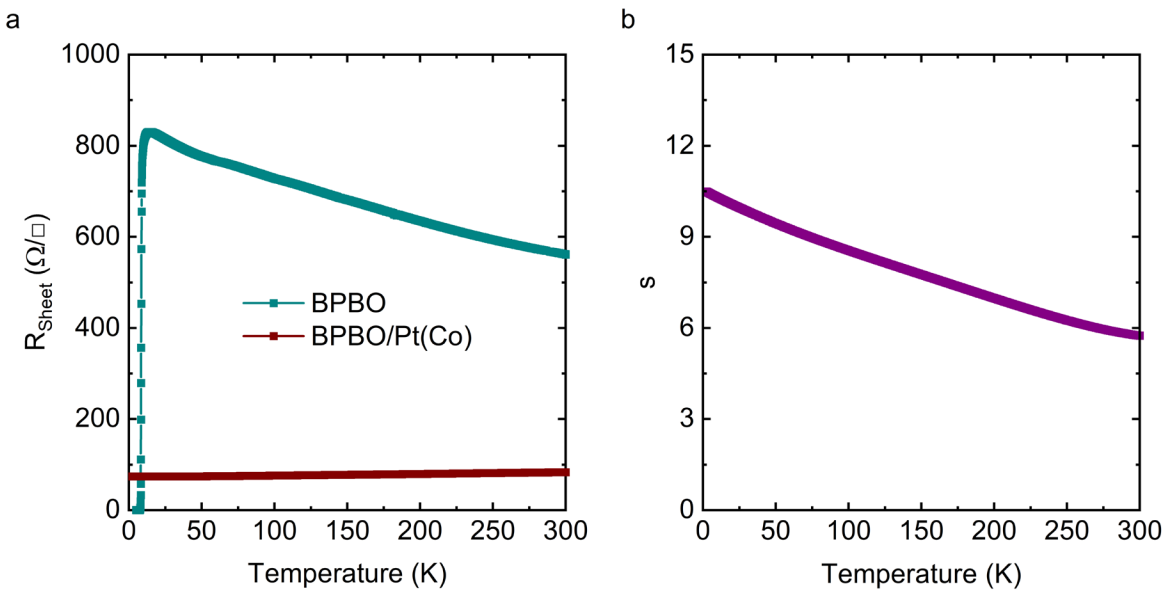

Figure S12 | Temperature dependent transport properties of BPBO and BPBO/Pt(Co). a, Sheet resistance of BPBO and BPBO/Pt(Co). **b,** Calculated Pt(Co) shunting factor.

Note 10. Comparison of spin source materials

In Table S1 we compare SOT figures of merit for BPBO to some of the most efficient spin sources for material systems including oxides, topological insulators, 2D materials, and heavy metals. Here, representative systems with reported PMA switching are considered for comparison.

Table S1| Comparison of SOT efficiency, θ_{SOT}, spin Hall conductivity, σ_{SH}, and critical current density for magnetization switching, j_{sw}, for several spin source materials. j_{sw} is the current density only through the NM layer.

Spin Source Material	θ_{SOT}	$\sigma_{SH}\left(10^5\frac{\hbar}{2e}\Omega^{-1}m^{-1}\right)$	j_{sw} (Acm^{-2})
$BaPb_{0.75}Bi_{0.25}O_3$ (this work)	2.7	2.6	4.0×10^5
$SrIrO_3$[9]	0.58	0.5	5.1×10^6
$Bi_xSe_{(1-x)}$[10]	18.62	1.5	4.3×10^5
WTe_2[11,12]	0.09	0.12	3×10^6
$Pt_{0.7}(MgO)_{0.3}$[13]	0.26	4	1.15×10^7
β-Ta[14]	-0.15	-0.8	8.6×10^6

References

1. Vanderbilt, D. Soft self-consistent pseudopotentials in a generalized eigenvalue formalism. *Phys Rev B* 41, 7892–7895 (1990).

2. Giannozzi, P., Baroni, S., Bonini, N., Calandra, M., Car, R., Cavazzoni, C., Ceresoli, D., Chiarotti, G. L., Cococcioni, M., Dabo, I., Corso, A. D., Gironcoli, S. de, Fabris, S., Fratesi, G., Gebauer, R., Gerstmann, U., Gougoussis, C., Kokalj, A., Lazzeri, M., Martin-Samos, L., Marzari, N., Mauri, F., Mazzarello, R., Paolini, S., Pasquarello, A., Paulatto, L., Sbraccia, C., Scandolo, S., Sclauzero, G., Seitsonen, A. P., Smogunov, A., Umari, P. & Wentzcovitch, R. M. QUANTUM ESPRESSO: a modular and open-source software project for quantum simulations of materials. *J Phys Condens Matter* 21, 395502 (2009).

3. Perdew, J. P., Burke, K. & Ernzerhof, M. Generalized Gradient Approximation Made Simple. *Phys Rev Lett* 77, 3865–3868 (1996).

4. Murnaghan, F. D. The Compressibility of Media under Extreme Pressures. *Proc National Acad Sci* 30, 244–247 (1944).

5. Nardelli, M. B., Cerasoli, F. T., Costa, M., Curtarolo, S., Gennaro, R. D., Fornari, M., Liyanage, L., Supka, A. R. & Wang, H. PAOFLOW: A utility to construct and operate on ab initio Hamiltonians from the projections of electronic wavefunctions on atomic orbital bases, including characterization of topological materials. *Comp Mater Sci* 143, 462–472 (2018).

6. Agapito, L. A., Ferretti, A., Calzolari, A., Curtarolo, S. & Nardelli, M. B. Effective and accurate representation of extended Bloch states on finite Hilbert spaces. *Phys Rev B* 88, 165127 (2013).

7. Agapito, L. A., Ismail-Beigi, S., Curtarolo, S., Fornari, M. & Nardelli, M. B. Accurate tight-binding Hamiltonian matrices from ab initio calculations: Minimal basis sets. *Phys Rev B* 93, 035104 (2016).

8. Karimeddiny, S., Mittelstaedt, J. A., Buhrman, R. A. & Ralph, D. C. Transverse and Longitudinal Spin-Torque Ferromagnetic Resonance for Improved Measurement of Spin-Orbit Torque. *Phys Rev Appl* 14, 024024 (2020).

9. Liu, L., Qin, Q., Lin, W., Li, C., Xie, Q., He, S., Shu, X., Zhou, C., Lim, Z., Yu, J., Lu, W., Li, M., Yan, X., Pennycook, S. J. & Chen, J. Current-induced magnetization switching in all-oxide heterostructures. *Nat Nanotechnol* 14, 939–944 (2019).

10. DC, M., Grassi, R., Chen, J.-Y., Jamali, M., Hickey, D. R., Zhang, D., Zhao, Z., Li, H., Quarterman, P., Lv, Y., Li, M., Manchon, A., Mkhoyan, K. A., Low, T. & Wang, J.-P. Room-temperature high spin–orbit torque due to quantum confinement in sputtered BixSe(1–x) films. *Nat Mater* 17, 800–807 (2018).

11. Shi, S., Liang, S., Zhu, Z., Cai, K., Pollard, S. D., Wang, Y., Wang, J., Wang, Q., He, P., Yu, J., Eda, G., Liang, G. & Yang, H. All-electric magnetization switching and Dzyaloshinskii–Moriya interaction in WTe2/ferromagnet heterostructures. *Nat Nanotechnol* 14, 945–949 (2019).

12. Kao, I.-H., Muzzio, R., Zhang, H., Zhu, M., Gobbo, J., Yuan, S., Weber, D., Rao, R., Li, J., Edgar, J. H., Goldberger, J. E., Yan, J., Mandrus, D. G., Hwang, J., Cheng, R., Katoch, J. & Singh, S. Deterministic

switching of a perpendicularly polarized magnet using unconventional spin–orbit torques in WTe2. *Nat Mater* 1–6 (2022). doi:10.1038/s41563-022-01275-5

13. Zhu, L., Zhu, L., Sui, M., Ralph, D. C. & Buhrman, R. A. Variation of the giant intrinsic spin Hall conductivity of Pt with carrier lifetime. *Sci Adv* 5, eaav8025 (2019).

14. Liu, L., Pai, C.-F., Li, Y., Tseng, H. W., Ralph, D. C. & Buhrman, R. A. Spin-Torque Switching with the Giant Spin Hall Effect of Tantalum. *Science* 336, 555–558 (2012).